Chemical Science

ROYAL SOCIETY OF CHEMISTRY

EDGE ARTICLE

View Article Online
View Journal

Cite this: DOI: 10.1039/d5sc07843a

All publication charges for this article have been paid for by the Royal Society of Chemistry

Highly-destabilized ligand field excited states of iron carbene complexes and their relation to charge transfer state lifetimes

Reagan X. Hooper, [a] Benjamin I. Poulter, [a] Jesper Schwarz, [b] Mariam Barakat,[c] Kristjan Kunnus,[d] Kacie J. Nelson,[a] Aleksandra Ilic, [b] Clara García-Mateos,[b] Rajdip Chowdhury,[b] Jens Uhlig, [e] Kenneth Wärnmark, [b] Elena Jakubikova, [c] Amy A. Cordones [a] and Kelly J. Gaffney *[a]

Lifetimes of photoexcited charge transfer (CT) states in transition metal chromophores are influenced by low-lying ligand field (LF) excited states, especially for 3d metal complexes. To manipulate interactions between LF and CT states, it is important to be able to control LF excited state energies using tunable synthetic variables. In this report, we use Fe 2p3d L_3-edge resonant inelastic X-ray scattering (RIXS) to measure LF excited state energies of three homoleptic iron chromophores coordinated by strong-field *N*-heterocyclic carbenes (NHCs). We investigate the effect of oxidation state and ligand scaffold on LF energies and covalency parameters. A cyclometalated bis(NHC) ligand affords both high LF excited state energies (and thus high 10 Dq) as well as high metal–ligand covalency compared to other iron complexes with very strong-field ligands. However, for the set of complexes investigated, we do not observe meaningful correlation between the LF excited state energies and the CT excited state lifetimes. These results illustrate that targeting long-lived CT excited states necessitates control of multiple molecular excited state properties, with destabilization of the LF excited state energies proving necessary, but insufficient, to control the CT excited state lifetime in Fe carbene complexes.

Received 10th October 2025
Accepted 14th December 2025

DOI: 10.1039/d5sc07843a

rsc.li/chemical-science

Introduction

Chemical potential derived from photoexcitation of molecular transition metal complexes has proven useful in areas such as solar energy harvesting,[5] pharmaceutical and natural product synthesis,[6,7] and laboratory-scale organic reactions.[9] Transition metal-based chromophores present the potential advantage of possessing a large number of structural variables, including metal identity and a multitude of ligand design choices. Understanding how this diversity affects electronic excited state properties is essential to utilizing all variables for synthetic benefit.

Many synthetic strategies for tuning excited state behavior have been explored in recent years.[10,11] Classically, long-lived charge transfer (CT) excited states of 4d and 5d metal complexes have been targeted due to their utility in photoredox catalysts.[12] For the more abundant and inexpensive 3d metals, reaching long CT excited state lifetimes proves more difficult. Compared to their 4d and 5d counterparts, 3d metal complexes have inherently weaker ligand fields (LF). These low-lying LF (equivalently metal-centered or d–d) excited states often act as efficient channels for non-radiative decay of CT excited states to the electronic ground state.[13] For this reason, many investigations have targeted ligands with strong σ-donation to generate larger LF splitting that impedes CT excited state relaxation through the manifold of LF excited states. The Wärnmark group has spearheaded the use of some of the strongest σ-donors available, *N*-heterocyclic carbenes (NHCs), in photoredox catalyst design.[1,14] In the decade since their original report, NHC ligands have been pivotal in achieving up to 190 nanosecond metal-to-ligand charge transfer (MLCT) lifetimes in third row transition metal complexes.[15–18] While a variety of ligand design approaches have been pursued to extend the CT lifetime of iron complexes, including increasing ligand steric strain[19] and inner coordination sphere symmetry,[20–22] increasing the LF strength has proven to be the most effective means of increasing CT excited state lifetimes. Systematic investigation of the correlation between CT lifetime and LF strength has never been reported due to the difficulty in measuring LF excited state energies (see below). Iron–NHC complexes are a good model

[a]*Stanford PULSE Institute, SLAC National Accelerator Laboratory, Menlo Park, CA 94025, USA. E-mail: kgaffney@slac.stanford.edu*

[b]*Centre for Analysis and Synthesis, Department of Chemistry, Lund University, Box 124, SE-22100 Lund, Sweden*

[c]*Department of Chemistry, North Carolina State University, Raleigh, NC 27695, USA*

[d]*Linac Coherent Light Source, SLAC National Accelerator Laboratory, Menlo Park, CA 94025, USA*

[e]*Division of Chemical Physics, Department of Chemistry, Lund University, Box 124, SE-22100 Lund, Sweden*

platform for examining this correlation between LF excited state energies and CT excited state lifetimes, since varying the strength of strong field ligands is a key facet in their design.

The successful implementation of NHCs in 3d metal photocatalysts warrants a more complete understanding of how they control CT excited state relaxation. Quantitative assessment of the degree of LF excited state destabilization by NHCs is needed to assess the relationship between the molecular complex structure and LF strength. Ideally, this information comes from direct measurement, as theoretical techniques are not yet able to reliably predict LF excited state energies for any arbitrary 3d metal complex.[23] Ultraviolet-visible absorption spectroscopy is the most accessible relevant technique, but LF transitions have weak molar absorptivity and often overlap with CT bands that have orders of magnitude higher absorption cross sections. These factors render the isolated observation of LF states impossible in the UV-visible absorption spectra of many systems, including Fe carbene complexes, though significant blue shifting of CT bands may enable some LF transitions to be resolved.[24] Transient absorption spectroscopy can sometimes observe differential changes that are attributed to changes to the LF states, but again struggle to identify their natures unambiguously.

Metal 2p3d L-edge resonant inelastic X-ray scattering (RIXS) spectroscopy measures the same LF states accessed by UV-visible absorption spectroscopy, also reporting them in the ground state geometry.[25] In contrast to the forbidden d–d transitions in the UV-visible range, resonant inelastic X-ray photon radiation scattering follows the selection rules of Raman scattering and takes advantage of allowed transitions between metal 2p and 3d orbitals, resulting in strong amplification of LF excited states relative to CT transitions in the final spectrum.[26] RIXS has therefore been an increasingly utilized technique for measuring LF excited state energies in photochemically interesting third-row metal complexes, where these energies may be inaccessible in the UV-visible absorption spectra.[2,27] In analogy to resonance Raman spectroscopy, RIXS first involves a metal 2p to 3d electronic excitation to a real core-hole excited state (comparable to the electronic excited state in the resonance Raman technique). Then this intermediate state decays *via* photon emission from a 3d electron re-filling the 2p hole, generating a final d–d excited state, analogous to the process in which an excited vibrational state in UV-visible resonance Raman scattering is formed. The difference in the X-ray absorption and emission energy is termed energy transfer, and in the case of effectively centrosymmetric complexes, energy transfer values map directly onto a Tanabe–Sugano diagram (Fig. 1). In addition to the strong intensities of LF excited states, the strong spin–orbit coupling in the 2p core hole state relaxes the spin selection rule for 2p3d RIXS, enabling LF excited states with $\Delta S \neq 0$ relative to the GS to be more intense than in a single-photon absorption spectrum.[28] Of note, since there is no 2p hole in the RIXS final state, the final state LF excited state energies are not affected by the core hole. This is in contrast to final states measured in metal L-edge XAS spectra, where simulation to derive parameters such as the ground state 10 Dq must assume that the observed excited state 10 Dq is reduced relative to the ground state, usually on the order of 10–20% for Fe–NHC complexes.[2,4] Thus, RIXS more directly measures the valence electronic structure of metal complexes than XAS.

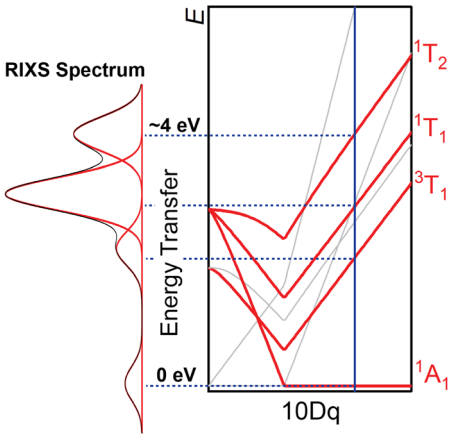

Fig. 1 Illustration of how metal L-edge RIXS features of a centrosymmetric complex can be mapped onto a Tanabe–Sugano diagram for a given 10 Dq and *B* (blue vertical line). The diagram shown is for an arbitrary octahedral d^6 complex and is not scaled in either axis by B^{-1}. The feature at zero energy transfer is the elastic line, and light grey lines represent additional low-lying LF excited states that are not typically resolved in RIXS experiments due to weak intensity and/or overlap with stronger features.

Iron–NHC complexes **1a**,[3] **1b**,[3,29] **2**,[17] and **3** (ref. 1) (Fig. 2) have been the subject of numerous previous studies for their potential as 3d metal photoredox catalysts, mainly using UV-visible transient absorption spectroscopy to understand their excited state behavior. In addition, **3** has already been studied using steady-state Fe L-edge RIXS as well as femtosecond-resolution X-ray emission and scattering to investigate the role of LF excited states in the excited state decay of low-lying metal-to-ligand (MLCT) states.[2,30] Complexes **1a** and **1b** are the ferrous[3] and ferric[3,29] cyclometalated versions of the first generation of Fe–NHC photosensitizers, namely the ferrous bis(NHC) complex (**3**)[1] with a central pyridine moiety instead of the cyclometalating central benzene ring. Cyclometalation of the NHC ligand is expected to raise LF excited state energies

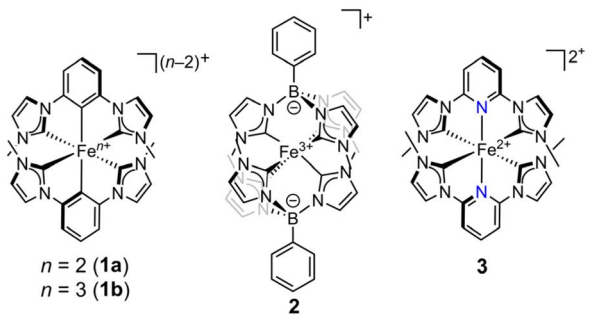

Fig. 2 Complexes with new RIXS analysis in this work (**1a**, **1b**, and **2**) and a closely-related complex (**3**) analyzed previously by Kunnus *et al.*[2] The counterion for complexes **1b** and **2** in our measurements was BPh_4^-, and it was PF_6^- for RIXS measurements of **3**.

because the anionic arene moiety is a stronger σ-donor than pyridine.[31] In spite of the predicted increase in LF induced by the arene donor, both of the iron(II) complexes (**1a** and **3**) have ^{3}MLCT excited state lifetimes of 9 ps.[1,3] Ferric complex **2** is structurally distinct, having two phenyl[tris(3-methylimidazol-2-ylidene)]borate (phtmeimb) ligands with low deviation of the inner coordination sphere from O_h symmetry (near 90 °C–Fe–C bond angles).[17] The iron(III) complexes (**1b** and **2**) have ^{2}LMCT lifetimes of 240 ps and 2 ns,[3,17,29] respectively, demonstrating how, within the class of NHC ligands, varying the backbone structure can have large effects on the CT excited state lifetimes.

Herein, we sought to quantify the LF excited state energies of **1a**, **1b**, and **2** to determine the extent to which variations in the LF excited state energies can be correlated with the ^{3}MLCT lifetimes of ferrous complexes **1a** and **3** and the ^{2}LMCT lifetimes of complexes **1b** and **2**. Additionally, from these LF excited state energies, we also extract 10 Dq and ground state covalency parameters. Overall, our study presents a comprehensive LF analysis of three Fe–NHC complexes on the cutting edge of iron CT excited state functionality, and we show how the isolated variables of oxidation state and ligand scaffold impact their ligand fields.

Results and discussion

Resonant absorption energies from Fe L_3-edge XAS

The first component of the RIXS process is a resonant X-ray excitation event, so understanding the structures of the L-edge XAS spectra is necessary for judicious selection of energies for RIXS measurements. The Fe L_3-edge XAS spectra for **1a**, **1b**, and **2** are plotted in Fig. 3. Experimental details can be found in SI Section II. The spectrum of **2** was already reported, and the energies and line shapes in our spectrum are consistent with literature for low-spin ferrous and ferric complexes.[4] Within this region, all complexes demonstrate a high-energy absorption with a maximum at 709.7 eV (**1a** and **1b**) and around 710 eV (**2**) (vertical dashed lines in Fig. 3). This absorption feature corresponds to transitions into states formed by Fe 2p→3d(e_g^*) absorption.[32] For ferric complexes **1b** and **2**, the t_{2g} orbital set also includes a single hole, and the lower-energy absorptions at 705.4 eV (**1b**) and 705.6 eV (**2**) represent states formed by Fe 2p → 3d(t_{2g}) absorption. This feature is well separated from the Fe 2p→3d(e_g^*) absorption line due to the strong ligand fields present in our complexes. Notably, the low-energy absorption is absent in the XAS spectrum of **1a**, suggesting minimal X-ray-induced photooxidation.[33]

States accessed by Fe 2p3d L_3-edge RIXS

Excitation energies that induce Fe 2p→3d(e_g^*) transitions result in intermediate RIXS states that can then form final states with LF excited state character: $(t_{2g})^5(e_g^*)^1$ for iron(II) and $(t_{2g})^4(e_g^*)^1$ for iron(III). For complexes **1a** and **1b**, the XAS spectra show a clear Fe 2p→3d(e_g^*) absorption maximum, while **2** has a more complex spectral shape, including a broad low-energy shoulder. In general, the e_g^* absorption envelope is broader for iron(III) complexes because of an increased number of microstates formed from the $(t_{2g})^5(e_g^*)^1$ valence intermediate state configurations relative to the $(t_{2g})^6(e_g^*)^1$ valence intermediate state configurations for L-edge absorption for low-spin iron(II).

We sought to better understand why the shape of the e_g^* resonance visibly differs between ferric complexes **1b** and **2** in order to better explain which intermediate states may be accessed by the L-edge absorption process. To do this, ligand field multiplet simulations were performed (SI Section III). These demonstrated that the splitting of the e_g^* peak is a function of Slater integral F_{dd}^k scaling (where lower F_{dd}^k is associated with increased covalency) when only the 3d–3d electron exchange and coulombic repulsion energies are considered (Fig. 4). This result suggests that the shape of the e_g^* XAS resonance is a consequence of covalency in this set of complexes. A more compact signal (as in **1a**) as opposed to a broad, unresolved, multi-peak structure (as in **2**) is a marker of increased metal–ligand covalency modeled as a reduction of 3d–3d electron repulsion (SI Section III). Below, we show how the X-ray absorption model guided the selection of incident energies and interpretation of RIXS spectra.

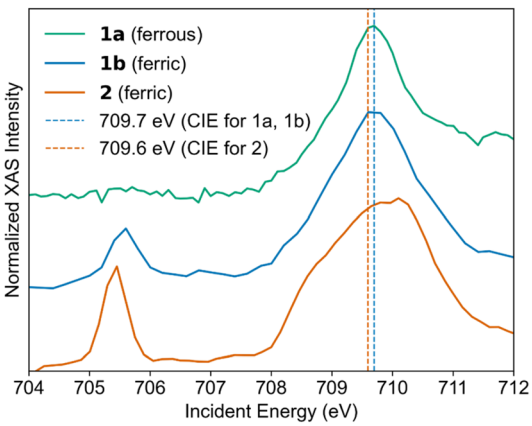

Fig. 3 Total electron yield Fe L_3-edge XAS spectra with vertical lines showing energies where constant incident energy RIXS spectra were fit.

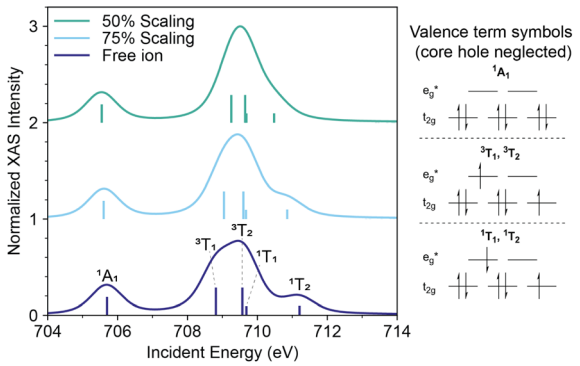

Fig. 4 Iron L_3-edge XAS simulations for a d^5 ground state (term symbols are for the d^6 final states, which are schematically represented on the right). A 10 Dq of 4.3 eV was used for all plots, and the intensity was normalized to the maximum value of the plot showing 50% scaling of the F_{dd}^k parameter.

The XAS spectra above provided a guide for the energy window to acquire two-dimensional RIXS maps across the Fe L_3-edge absorption envelope. Collection of full RIXS maps is generally not required to pick resonant absorption energies, as these can be designated based on the XAS spectra. However, we chose to report and discuss the 2D RIXS maps to demonstrate the additional information that can be gained from their analysis and to thoroughly illustrate the concept of constant incident energy (CIE) RIXS spectra, from which LF excited state energies were extracted.

In our 2D RIXS maps, the *x*-axis shows the incident energy used to excite an L-edge XAS transition, and the *y*-axis shows energy transfer (the Raman shift determined by subtracting the energy of the inelastically scattered photon energy from the incident photon energy to provide the energy of the electronic excited state created by RIXS, often referred to as the final state). We indicate intensities of RIXS final states as a color map. The 2D RIXS map of complex **2** is shown in Fig. 5. By summing the RIXS intensities along the energy transfer axis, an L-edge-like spectrum is obtained (PFY trace in Fig. 5). Vertical cuts at a constant incident energy more clearly show LF excited state energies. All of our RIXS maps have intense LF excited state resonances and variable degrees of intensity for the weaker elastic bands and high energy transfer features which result from a complex combination of CT and high-energy LF excited states.[2,28] Fig. S3 shows a labeled description of the RIXS map of **2**. Focusing on the lower energy t_{2g} resonance, the primarily inelastic scattering channel creates CT final states of LMCT character, whose intensities reflect the amount of metal character in the occupied ligand-based orbitals from which the electron that fills the Fe 2p core hole originates.[26] An example of such a state is the ~4 eV transfer peak at a ~705.5 eV incident energy in the RIXS map of **2** (Fig. 5). Moving to the intense higher-energy e_g^* region of this RIXS map centered around 709.5 eV, it is also notable that multiple maxima are observable in the low-lying LF excited state region (3 to 6 eV), whereas the XAS spectrum of **2** does not resolve any fine structure. This result demonstrates the ability of 2D maps to resolve XAS resonances by extending an incident energy *vs.* intensity plot (XAS) to one with a third dimension of energy transfer.

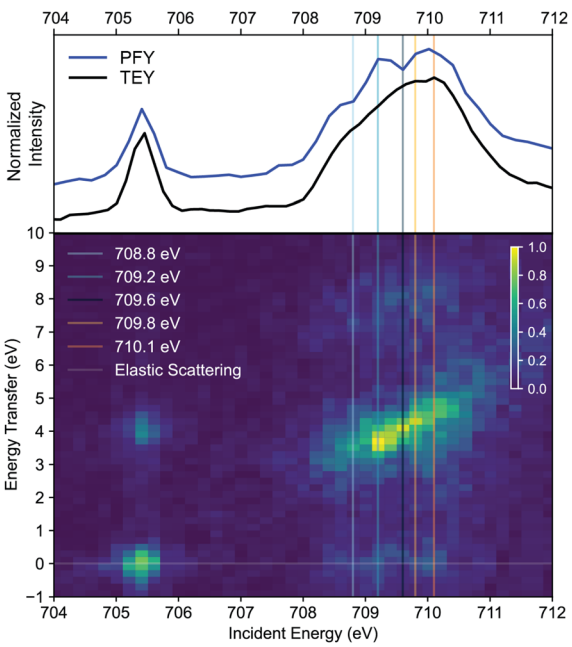

Fig. 5 Maximum-intensity-normalized 2D RIXS map of ferric complex **2** at the L_3 absorption edge. PFY = partial fluorescence yield spectrum from integrated RIXS map. TEY = total electron yield spectrum from XAS. The vertical lines in the 709 to 710 eV area show the energies where CIE RIXS spectra were measured and averaged.

Derivation of ligand field energies from RIXS spectra

Constant incident energy (CIE) RIXS spectra were analyzed for the purpose of obtaining LF excited state energies. Briefly, energies were chosen to be resonant with 2p3d absorptions involving an excitation into an e_g^* orbital, giving final states of LF character. A full description of how the energies were chosen is given in SI Section II.

Many methods for assigning LF excited states to transition metal L-edge RIXS features have been reported in the literature. These include high-level *ab initio* calculations,[2,28,34–36] charge transfer multiplet (CTM) calculations that fit both LF (10 Dq and Racah *C* and *B*) and charge transfer parameters,[2,25,27,35] and several variations of fitting that use only LF parameters.[25,27,28,37] There are advantages and disadvantages to each approach, and for different systems it may be appropriate to use different methods. While *ab initio* calculations are not affected by experimental constraints such as resolution, accuracy may be an issue, and a potential need for very large active spaces can render their cost prohibitively high. CTM calculations are semi-empirical in nature and parameterize both the crystal field and its mixing with MLCT and LMCT states, providing a comprehensive model.[38] They are particularly useful when CT mixing effects are significant, such as in iron hexacyanide complexes.[35,39] Given the large number of parameters, challenges of using CTM theory include overparameterization and the consideration that the parameter space combined with spectral resolution generally does not allow for a unique fit. The third listed method, in which RIXS spectra are interpreted through only the lens of LF theory, typically uses fewer parameter inputs and is a time-tested tool on UV-visible absorption spectra. This aspect gives it the advantage of direct comparison to literature published prior to the development of quantum chemical and CTM methods. A major limitation of the LF theory approach is the restricted symmetries to which existing full models can be applied, but our complexes are satisfactorily approximated by a point group (O_h) which can be rigorously treated (see SI Section IV).

Consequently, we have chosen to interpret our RIXS spectra using LF theory. The single primary peak of the ferrous L_3-edge XAS spectrum of **1a** along with absence of obvious satellite features (Fig. 3) suggests that mixing of CT and LF states is negligible, and thus CTM treatment offers little additional advantage with the risk of overparameterization. The shapes of the ferric L-edge XAS spectra are adequately described using only LF multiplet simulations (Fig. 4), and are again lacking in

strong satellite features arising from highly-covalent CT transitions. The foundation of the LF theory fitting procedure is matrices describing total valence d electron–electron repulsion, in terms of the octahedral LF splitting 10 Dq, and Racah parameters *B* and *C*, reported by Tanabe and Sugano, from which the eponymous diagrams are derived.[8,40]

Modeling method and uncertainty

To obtain LF parameters from CIE RIXS spectra fitting, we adapted a fitting code from previous reports by Kunnus *et al.* and Larsen *et al.*,[27,41] which performs least-squares fitting of LF energies by varying the LF parameters 10 Dq, *C* and *B* that are embedded within the Tanabe–Sugano matrices. SI Section IV discusses the justification of this choice compared to direct selection of LF state energies from the RIXS spectra. Parameters *C* and *B* are derived directly from the more fundamental Slater integrals F^2 and F^4, whose changes represent the degree of isotropic radial d electron expansion that occurs at a metal site upon formation of a metal–ligand bond.[42] One notable difference between the fit code used by Larsen *et al.*[27] and the one used herein is that the scaling of both F^2 and F^4 was uniform in the former, while we allowed them to scale independently. Uniform $F_{dd}{}^k$ scaling results in the ratio *C*/*B* being fixed to the free ion constant value of 3.73 (eqn (S1) and (S2)). A *C*/*B* ratio fixed to the free ion value is commonly adopted, though there is physical justification for the ratio *C*/*B* to be variable across systems (SI Section IV);[42] therefore, we favored a variable *C*/*B* ratio, though we also compare to fits where we enforce a *C*/*B* value of 3.73.

The spectral resolution is not sufficient to manually distinguish individual peaks in our systems that have high densities of energetically-close LF excited states. Peak fitting methods therefore do not give unique results, adding uncertainty to the LF state energies. In the most extreme case, the inaccuracy of an individual LF state energy is estimated to be maximally 0.5 eV relative to its true value, based on differences using fixed *vs.* free *C*/*B* values for the RIXS spectrum of **1a**, which both gave acceptable fits (Table S3). To investigate the precision of our fit-derived LF parameters, we sampled the parameter space for the floated *C*/*B* model using bootstrap methods (SI Section IV and Table S5). The major conclusions from bootstrapping are that differences in 10 Dq are statistically significant but that values of *B* and *C* are less precise. The latter observation is likely because both varied *C*/*B* and fixed *C*/*B* give reasonable fits to our data (Fig. 6), though we prefer the physical model of varied *C*/*B*. Several aspects increase confidence in both the fits and the conclusions drawn on them: (1) the LF energies are constrained to a physical model; (2) the LF strengths and energies have a large distribution between complexes such that firmly assigning order is possible; and (3) the most intense states in each fit have the same multiplicity as the ground state ($\Delta S = 0$), which is consistent with previous RIXS studies and physical expectations.[25,36]

Ligand field excited state energies of 1a and 1b

The fits for **1a** and **1b** CIE RIXS spectra at 709.7 eV (Fe 2p → 3d(t_{2g}) absorption) are shown in Fig. 6a and b and their state energies in Table S4. For **1a**, the main contributor to the RIXS spectrum is assigned to a $^1T_1$ final state, in agreement with previous RIXS studies of six-coordinate iron(II) with similarly strong-field ligand environments (Fig. 6a).[2,35] The $^1T_1$ state resonance of **1a** appears at 4.2 eV, which is about 1 eV higher than the analogous state in its pyridine analogue (complex **3**),[2] showing that the central arene induces a much stronger LF than the central pyridine donor of **3**. The lowest-energy LF excited state, $^3T_1$, is observed as a weak low-energy (3.35 eV) shoulder of $^1T_1$. Intensity at the weak shoulder could only be accounted for by variable *C*/*B*, as a fixed value of 3.73 gave a $^3T_1$ energy of 3.65 eV (Fig. 6a). Fitting a lower energy to the $^3T_1$ state not only better reproduces the experimental spectra but is also in closer alignment with previously-calculated theoretical vertical transition energies, which shows a $^3T_1$ energy of ∼2.9 eV for **1a**.[3] Comparison between computed and measured $^3T_1$ energies for **3** also reveals a discrepancy of similar magnitude (∼0.5 eV, where the calculated value is lower).[2,43]

The RIXS spectrum of **1b** has a more complicated structure, with major contributions from formally spin-allowed doublet states, specifically the lowest-lying ^2E state around 4.3 eV (Fig. 6b). In the RIXS experiments, excitation into the e_g^* orbitals produces final states of $t_{2g}{}^5e_g^{*1}$ for ferrous **1a** and $t_{2g}{}^4e_g^{*1}$ for ferric **1b**. Within the strong field O_h framework and ignoring spin–orbit coupling, there are 24 microstates possible for the iron(II) $t_{2g}{}^5e_g^{*1}$ configuration and 60 for the iron(III) $t_{2g}{}^4e_g^{*1}$ configuration, leading to more possible terms in the ferric RIXS spectra fits.[44] As pointed out above, the experimental resolution does not permit parameter-free fitting of well-defined peaks. Although it may be possible to manually fit the spectra with fewer Gaussians, the number of states are defined by LF theory, and previous RIXS studies indicate that all may contribute to the experimental spectra with incident energy intensity dependence.[28] For **1b**, DFT-calculated values of the lowest LF excited state ($^4T_1$, 3.14 eV) range from about 2 eV to 2.6 eV depending on the method used, and this is about 0.5–1.0 eV lower than what is observed experimentally.[3,29]

Ligand field excited state energies of 2

The fit of the RIXS spectrum of **2** at a CIE of 709.6 eV is shown in Fig. 6c and state energies in Table S4. Similar to the other ferric complex **1b**, these fits indicate that the major contribution to the spectrum at the e_g^* absorption resonance is the lowest-energy ^2E state. Compared to **1b**, the intensities of other states in complex **2** are diminished at a 709.6 eV CIE spectrum. After fitting the RIXS spectrum of **2** at 709.6 eV, the positions of the LF energies from this fit were then used to fit RIXS spectra at additional CIEs (marked in Fig. 5 as vertical lines), keeping LF energies constant and only changing their intensities (Fig. S8). At these additional cuts, RIXS states other than ^2E gain relative intensity. The adequate fits of RIXS spectra at different CIEs spanning the e_g^* absorption region using fixed final state energies show the robustness of the LF excited state energies from the initial fit in Fig. 6c. The lowest LF excited state, $^4T_1$, fit to an energy of 2.33 eV, is in decent agreement with the DFT-calculated value of 2.19 eV.[17]

Ligand field parameters. The LF parameters 10 Dq, *B*, and *C* represent the condensed sum of many distinct physical effects,

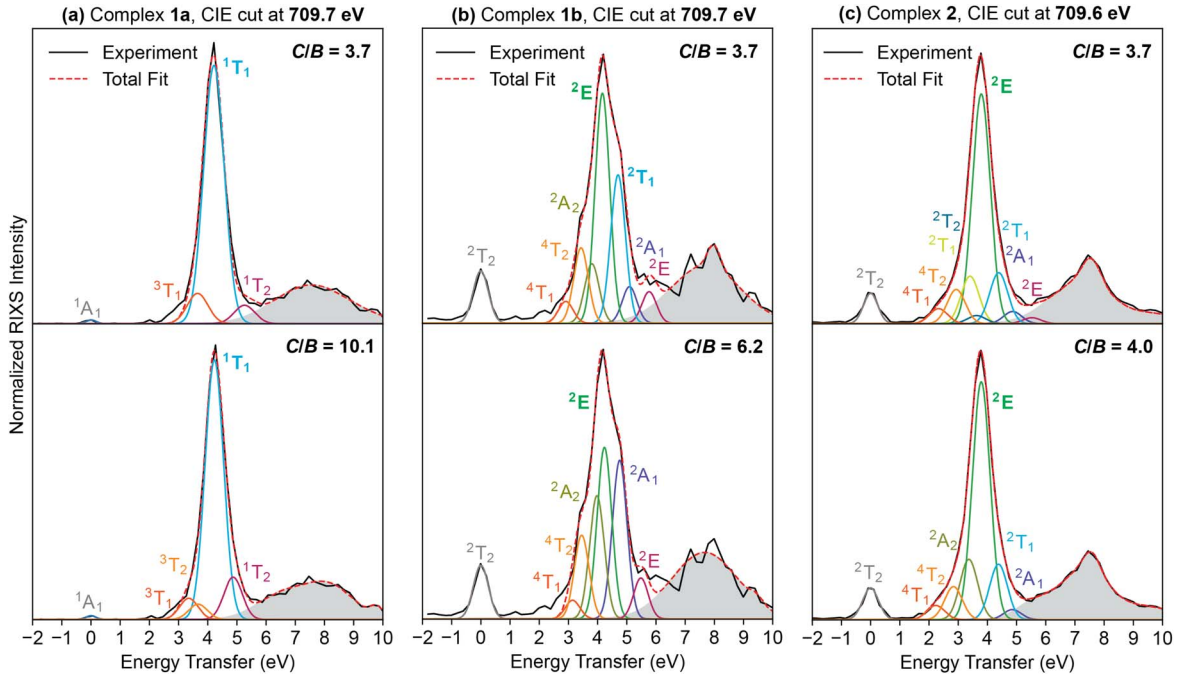

Fig. 6 Ligand field excited state energy fitting of RIXS cuts at CIE energy of 709.7 eV for complexes **1a** and **1b** and at 709.6 eV for **2**. The fitted peak at zero energy transfer represents elastic scattering and is labeled as the ground state term symbol. Elastic scattering linewidths: 0.9 eV (**1a**), 0.6 eV (**1b**), 0.6 eV (**2**); inelastic scattering linewidths: 0.4 eV (**1a**), 0.6 eV (**1b**), 0.7 eV (**2**). The grey region represents CT or higher-lying LF states and is modeled in the least squares fitting by up to four Gaussian-shaped bands. The *C*/*B* ratio was fixed at 3.73 in the top panels and was floated in the lower panels. Some states have negligible fit intensity in certain fits (see Tables S3 and S4).

but they provide a set of readily comparable values by which LF strength (10 Dq) and covalency (*C* and *B*) can be compared between compounds to help rationalize differences in their excited state properties. The importance of the LF strength in promoting long-lived CT excited states is well known, and in recent years, tuning metal–ligand covalency has been explored as an avenue to alter excited state properties.[27,45,46] Since the floated *C*/*B* fit is considered to be more physically accurate, the LF parameters discussed next include variable *C*/*B* ratio fits, unless otherwise specified.

Ligand field strength. Relevant parameters both with and without floated *C*/*B* are listed in Table 1. The 10 Dq value of **1a** was found to be 4.6 eV. This is markedly increased relative to other iron complexes with strong field ligands such as its pyridine analogue **3** (2.7 eV), other ferric and ferrous homoleptic iron carbene complexes (3.2–3.8 eV), $[Fe(CN)_6]^{4-}$ (4.2 eV), and $[Fe(CN)_6]^{3-}$ (4.3 eV).[4,47] The large 10 Dq of **1a** suggests that the M–L σ orbitals of the of **1a** are highly destabilized due to the two anionic arene donors. The ferric complex **1b** has a 10 Dq value of 4.3 eV, which is comparable to ferricyanide.[47] While LF strength usually increases with increasing oxidation state, the opposite effect is observed for **1a** and **1b** in both fitting models.[44] This trend opposing the norm is attributed to a bond length expansion for the Fe–C(carbene) bonds upon oxidation state change from iron(II) in **1a** to iron(III) in **1b**.[29] The Fe–C(arene) bond lengths between the two compounds show no statistical difference. Comparisons of density functional theory (DFT) generated molecular orbitals (MOs) of **1a** and **1b** (Fig. S10) indicate that the electron hole formed upon oxidation of ferrous **1a** resides in a MO that has some weak Fe–C π bonding interaction, and thus ferric **1b** might have a decreased Fe–C(carbene) bond order relative to **1a**.

The 10 Dq value of **2** is 3.8 eV in both fit models. This is consistent with the ground state 10 Dq parameter obtained from fitting the Fe L-edge XAS spectrum of **2** with charge transfer multiplet calculations in a previous report from Uhlig *et al.*[4] The smaller LF of **2** *versus* **1b** is surprising given its near 90 °C–Fe–C bond angles that would be expected to raise 10 Dq.[48,49] A potential contributor to the smaller LF of **2** is that its Fe t_{2g} orbitals do not appear to engage in as much π bonding with carbene π* orbitals (Fig. S11) as in **1b**, which has clearer Fe–C π back bonding that may lower its t_{2g} orbital energies (Fig. S10).

Covalency

The ability of metal–ligand covalency to affect LF excited state energies is illustrated in commonly-known Tanabe–Sugano diagrams, where both the energy and 10 Dq axes are scaled by B^{-1}.[8] In Fig. S7, plots of LF excited state energies as a function of covalency (represented by uniform scaling of the $F_{dd}{}^{k}$ parameters) clearly convey that for a given 10 Dq, $F_{dd}{}^{k}$ scaling may have considerable effects on LF state energies. It is this dependence that makes covalency a viable tuning point for LF excited state energetics, independent of the LF strength that is most commonly considered. Covalency is most often compared using the nephelauxetic parameter β which is equivalent to $B_{complex}/B_{free\ ion}$, where a lower value is assumed to indicate greater covalency. This parameter should be used with caution, however, as eqn (S3) shows that when *C*/*B* is not fixed between

Table 1 Summary of photochemically-relevant LF energies and parameters. The first three lines of data are from fits where C/B was allowed to float, and the three lower lines are from fixed C/B

Complex	GS	Lowest LF excited state (energy, eV)	10 Dq (eV)	B (cm^{-1}, eV)	C (cm^{-1}, eV)	C/B	β	$C/C_{free\ ion}$
1a	$^1A_1$	$^3T_1$ (3.35)	4.6	346, 0.0429	3490, 0.4327	10.1	0.38[b]	0.86
1b	$^2T_2$	$^4T_1$ (3.14)	4.3	325, 0.0403	2023, 0.2509	6.2	0.32[b]	0.42
2	$^2T_2$	$^4T_1$ (2.33)	3.8[a]	643, 0.0797	2600, 0.3224	4.0	0.63[b]	0.54
1a	$^1A_1$	$^3T_1$ (3.67)	4.4	579, 0.0718	2138, 0.2650	3.7	0.63	0.53
1b	$^2T_2$	$^4T_1$ (2.91)	4.2	436, 0.0541	1626, 0.2016	3.7	0.43	0.34
2	$^2T_2$	$^4T_1$ (2.23)	3.8[a]	512, 0.0634	1908, 0.2366	3.7	0.50	0.40

[a] Values are consistent with prior literature.[4] [b] These 'β' values are not directly comparable. $\beta = B_{complex}/B_{free\ ion}$ (for $C/B = 3.73$, these are comparable). $B_{free\ ion}$ values used: 917 cm^{-1} (iron(II)), 1015 cm^{-1} (iron(III)).[8] $C_{free\ ion}$ values used: 4040 cm^{-1} (iron(II)), 4800 cm^{-1} (iron(III)).[8]

complexes, $B_{complex}$ is a function of C/B. Thus, β should only be compared when C/B is fixed across samples. The β parameters (for $C/B = 3.73$) and B values (for floated C/B) for complexes **1a** and **1b** are significantly reduced compared to relevant ferrous and ferric comparisons, including **2**.[2,27,28,50] In general, these results show that the covalency imparted by the cyclometalated NHC ligand is substantial.

Although a complete physical interpretation of covalency is complicated by anisotropic metal–ligand interactions as well as the dual effects of electrostatic screening (central field covalency) and delocalization of metal d orbitals in the formation of molecular orbitals,[51,52] we were able to assess delocalization due to bonding using DFT-generated orbital pictures in Fig. S10 and S11. These show that **1b** generally has less than about 50 percent iron character (and conversely a high percent of ligand character) in the valence orbitals possessing metal-derived d-orbital symmetry, indicating highly-covalent bonding that disperses iron d electrons across the ligands.[53] While **2** also features some molecular orbitals with close to 50 percent or lower Fe d-orbital parentage, its occupied t_{2g} orbital set is markedly more ionic than that of **1b**, due to fewer metal–ligand π interactions as mentioned above (Fig. 7). These DFT findings are complimentary to the experimental ratios of F^2/F^4 for **1b** and **2**, which are consistent with **1b** having an extended π system and **2** having π orbitals but no large conjugated π network (SI Section V).[54] Within this set of complexes, covalency appears to be mainly governed by metal–ligand π bonding, where the large degree of π conjugation in **1b** correlates with enhanced covalency compared to **2**.

Ligand field excited state energies and CT lifetimes

Understanding the interactions of LF and CT excited states is essential to fully harnessing 3d metal complexes for photochemical applications, and so we examined the potential connections between LF energies measured by RIXS and previously-reported CT excited state kinetics studies on the iron complexes herein. The lowest-energy LF excited state ($^3T_1$) for ferrous cyclometalated bis(NHC) complex **1a** was found to be 3.35 eV in this study, while its pyridine bis(NHC) counterpart **3** has a $^3T_1$ energy of 2.45 eV (Fig. 8).[2] Despite the much stronger LF of **1a**, both have a dark ^{3}MLCT state with a 9 ps lifetime, suggesting different mechanisms for decay of the ^{3}MLCT state.[1,55] For **3**, ultrafast X-ray emission spectroscopy experiments demonstrated that the 9 ps time constant corresponds with ^{3}MLCT → ^{3}LF internal conversion,[23] while for **1a**, the 9 ps time constant is proposed from calculations to originate from direct ground state recovery *via* the ^{3}MLCT state.[3] Our RIXS measurements show that the $^3T_1$ energy is above the rather high ^{3}MLCT energy of ~2.5 eV in the ground state geometry of **1a**, but previous calculations suggest that the relaxed $^3T_1$ geometry could have a lower energy than the ^{3}MLCT state, adding internal conversion to ^{3}LF as another potential decay route.[3] Achieving long-lived MLCT states in iron(II) species has largely proven a formidable goal, with the first reported major advancement toward ns lifetimes being accomplished using a homoleptic bis(1,2,3-triazol-5-ylidene) complex.[56] Three iron(II) complexes have a reported MLCT lifetime of at least 1 ns at room temperature, with one featuring a cyclometalated phenanthroline ligand (noting that some long-lived excited states of iron(II) species initially assigned as MLCT were later evidenced to be ^{5}LF in nature).[57–60] Calculations on the cyclometalated complex showed that the ^{3}LF state energy was above the lowest ^{3}MLCT state after nuclear relaxation, due to the combination of its strong LF and very low ^{3}MLCT energy (~1.1 eV).[61] Clearly, a challenge in the design of next generation iron(II) MLCT catalysts is to achieve a balance between both high-energy LF excited states and high-energy, long-lived MLCT states. For iron(II) complexes, perhaps targeting long-lived MC excited states is a worthwhile endeavor.

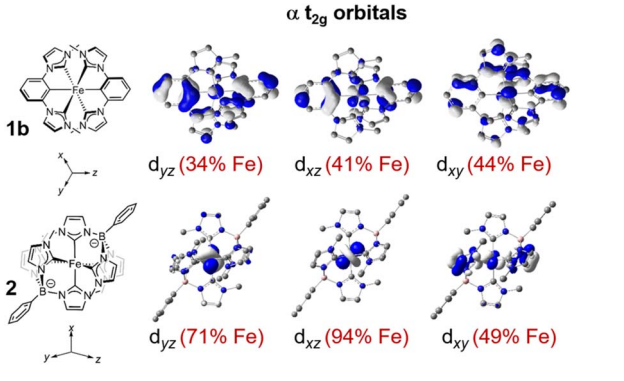

Fig. 7 Comparison of DFT-derived t_{2g} orbital makeup of ferric **1b** and **2**, showing increased covalency for **1b** compared to **2**. The full orbital diagrams are shown in Fig. S10 and S11.

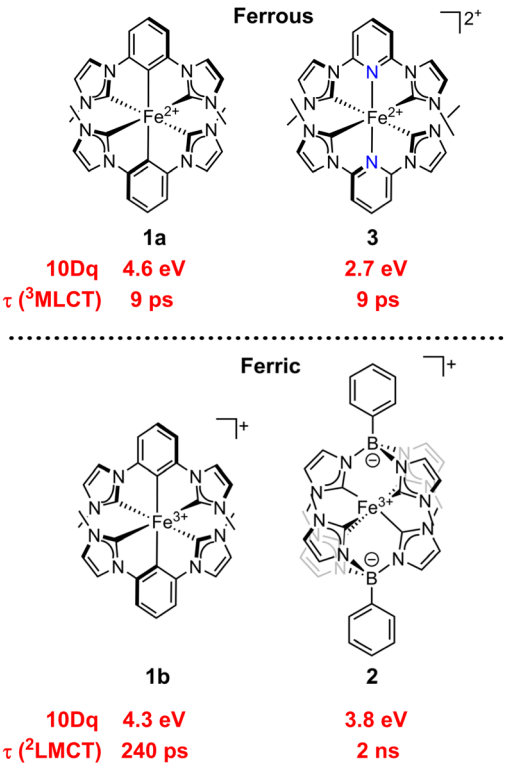

Fig. 8 Chart of 10 Dq, CT excited state lifetimes, and CT excited state energies for the complexes with RIXS reported here (**1a**, **1b**, and **2**) as well as a highly comparable complex (**3**) with LF excited state energies known from previous RIXS studies.[1,2]

In contrast to the ^{3}MLCT states of iron(II) NHC complexes, iron(III) NHC complexes have low-energy ^{2}LMCT states with a stronger record of favorable photoredox properties, including longer-lived and higher-energy CT states.[16,17,62,63] We measured the LF excited state energies of two ferric complexes with significantly different ^{2}LMCT lifetimes: **1b** ($\tau = 240$ ps)[3,29] and **2** ($\tau = 2$ ns)[17] (Fig. 8) but comparable LMCT energies. Interestingly, we found that **1b** has a stronger LF than **2**, with the lowest measured LF excited state energy ($^2T_2$) of **1b** being about 0.8 eV higher than that of **2**. While an explanation of this finding is outside the scope of this article, it illustrates that, once a complex is well into the strong LF regime, additional factors, like the magnitude of the intramolecular reorganization energy and the strength of the non-adiabatic coupling between the LMCT and ground electronic states, may dictate the LMCT lifetimes of ferric species. A recent example from Wenger *et al.* amplifies the notion that aspects other than LF energies mainly control ^{2}LMCT lifetimes in very strong-field cases. They reported an iron(III) NHC complex with the same structural backbone as the ligand in **1a**/**1b** but with an attached organic chromophore.[16] Those changes should not greatly affect the already very large 10 Dq afforded by the cyclometalated NHC, yet the ^{2}LMCT lifetime of their iron(III) complex is 100 ns, compared to 240 ps for **1b**, as the attached organic chromophore acts as a triplet reservoir.[16] Evidence for pure distal substituent effects on the LMCT lifetimes of **1b** derivatives has also been recently disclosed, citing differences between decay mechanisms tuned by the LMCT energy as the major contributor.[64]

The CT energies for all of the complexes in Fig. 8 lie within a narrow range of *ca.* 1.9–2.1 eV.[3,17,65] For **1a** and **3**, identical ^{3}MLCT lifetimes combined with large energy differences between their lowest LF excited states and ^{3}MLCT states might result from different mechanisms for ^{3}MLCT decay. While it is known that the 9 ps lifetime ^{3}MLCT state of **3** is deactivated partially through population of a lower-lying ^{3}MC state,[30] it is possible that the ^{3}MLCT state of **1a** primarily decays directly to the ground state.

Assuming that the geometrically-relaxed $^4T_1$ state for **1b** and **2** is lower in energy than their ~2 eV ^{2}LMCT state (corroborated through previous calculations),[3,17] a larger driving force and thus larger rate constant for $^2\text{LMCT} \rightarrow {}^4T_1$ should be present for **2** in the Marcus normal region.[66] We therefore speculate that the long lifetime of **2** could be due to unmeasured effects such as ^{2}LMCT and ground state wavefunction overlap that influences the non-adiabatic coupling between these electronic states.

Conclusions

Iron 2p3d L-edge RIXS was used to measure the low-lying ligand field excited state energies of three Fe–carbene complexes, and the effects of oxidation state and ligand structure on LF splitting and covalency parameters were evaluated. Our extensive analysis of LF parameters contributes to a growing interest in controlling 3d transition metal excited state behavior by tuning covalency, showcasing the remarkable LF properties of highly-covalent, strongly-donating NHC complexes. Several conclusions relating ground state molecular structure and excited state electronic structure of Fe–NHC complexes can be drawn from our findings.

First, the cyclometalated NHC ligand in **1a** and **1b** imparts some of the strongest ligand fields known for ferrous and ferric complexes, while the phtmeimb ligand in **2** is comparably weaker despite forming complexes with less deviation from O_h symmetry about the metal. An unusual reversal of the trend of higher oxidation state leading to larger 10 Dq is observed for the **1a**/**1b** redox pair. Secondly, comparison of both ferrous (**1a** compared to **3**) and ferric (**1b** compared to **2**) Fe–carbene complexes supports the conclusion that increasing the LF excited state energies above the low-lying CT excited states presents a necessary but insufficient pathway to increasing CT lifetimes. Incorporating this important finding into the design of next generation iron photosensitizers will be a challenging task, requiring careful consideration of all factors governing electron transfer rates. Based on the highly-speculative factors driving the relationships between LF energies and CT lifetimes in this study, it may be particularly important to control rates of direct CT to ground state deactivation through modification of CT excited state energy, as well as the degree of ground and excited state electronic coupling.

Overall, our study highlights the current potential for steady-state metal L-edge RIXS to characterize the ground state ligand fields of photochemically-important systems. These descriptions are essential for understanding how to modulate fundamental yet experimentally difficult-to-quantify aspects of metal–ligand interactions such as their strength and covalency. Some

tentative inferences regarding excited state dynamics could be made from our data, which may stimulate further studies. Going forward, we expect that steady-state and time-resolved RIXS spectroscopy will continue to provide unique insights, facilitating discovery of thus far unrecognized factors that control the interaction of molecular transition metal complexes with light.

Author contributions

KJG conceptualized of the project aims. JS, AI, CGM, and RC synthesized the complexes. RXH, BIP, KJN, and KK contributed to beam time data collection. BIP provided scripts for processing the data and assisted RXH in performing ligand field multiplet simulations. MB performed and analyzed the DFT calculations. RXH prepared the samples for X-ray measurements, collected and analyzed the data, and wrote initial drafts of the manuscript. KW, EJ, JU, AAC, and KJG secured funding, supervised the research, and provided guidance in data analysis. All authors participated in preparation of the final manuscript.

Conflicts of interest

There are no conflicts to declare.

Data availability

All X-ray spectroscopic data is available in the Zenodo repository at https://doi.org/10.5281/zenodo.17308224.

Supplementary information (SI): synthetic and X-ray measurement methods, further discussions about data analysis, and details about DFT calculations. See DOI: https://doi.org/10.1039/d5sc07843a.

Acknowledgements

Research was supported as part of BioLEC, an Energy Frontier Research Center funded by the U.S. Department of Energy (DOE), Office of Science, Basic Energy Sciences (BES), under Award no. DE-SC0019370. This research used resources of the Advanced Light Source, a U.S. DOE Office of Science User Facility under contract no. DE-AC02-05CH11231. We thank Dr Wanli Yang and Dr Gi-Hyeok Lee for providing experimental support at the Advanced Light Source. KW acknowledges support from the Swedish Strategic Research Foundation (EM16-0067), Knut and Alice Wallenberg Foundation (2018.0074), the Swedish Research Council (VR 2020-03207), the Swedish Energy Agency (Energimyndigheten, P48747-1), and the LMK Foundation. JS acknowledges support from the Royal Physiographic Society of Lund. JU acknowledges support from the Swedish Research Council (VR 2020-04995).

References

1 Y. Liu, T. Harlang, S. E. Canton, P. Chábera, K. Suárez-Alcántara, A. Fleckhaus, D. A. Vithanage, E. Göransson, A. Corani, R. Lomoth, V. Sundström and K. Wärnmark, *Chem. Commun.*, 2013, **49**, 6412–6414.
2 K. Kunnus, M. Guo, E. Biasin, C. B. Larsen, C. J. Titus, S. J. Lee, D. Nordlund, A. A. Cordones, J. Uhlig and K. J. Gaffney, *Inorg. Chem.*, 2022, **61**, 1961–1972.
3 C. E. Johnson, J. Schwarz, M. Deegbey, O. Prakash, K. Sharma, P. Huang, T. Ericsson, L. Häggström, J. Bendix, A. K. Gupta, E. Jakubikova, K. Wärnmark and R. Lomoth, *Chem. Sci.*, 2023, **14**, 10129–10139.
4 M. Guo, R. Temperton, G. D'Acunto, N. Johansson, R. Jones, K. Handrup, S. Ringelband, O. Prakash, H. Fan, L. H. M. de Groot, V. F. Hlynsson, S. Kaufhold, O. Gordivska, N. Velásquez González, K. Wärnmark, J. Schnadt, P. Persson and J. Uhlig, *Inorg. Chem.*, 2024, **63**, 12457–12468.
5 C. E. Housecroft and E. C. Constable, *Chem. Sci.*, 2022, **13**, 1225–1262.
6 P. Li, J. A. Terrett and J. R. Zbieg, *ACS Med. Chem. Lett.*, 2020, **11**, 2120–2130.
7 T. P. Nicholls, D. Leonori and A. C. Bissember, *Nat. Prod. Rep.*, 2016, **33**, 1248–1254.
8 Y. Tanabe and S. Sugano, *J. Phys. Soc. Jpn.*, 1954, **9**, 766–779.
9 C. K. Prier, D. A. Rankic and D. W. C. MacMillan, *Chem. Rev.*, 2013, **113**, 5322–5363.
10 G. Morselli, C. Reber and O. S. Wenger, *J. Am. Chem. Soc.*, 2025, **147**, 11608–11624.
11 D. Kim, V. Q. Dang and T. S. Teets, *Chem. Sci.*, 2024, **15**, 77–94.
12 A. Y. Chan, I. B. Perry, N. B. Bissonnette, B. F. Buksh, G. A. Edwards, L. I. Frye, O. L. Garry, M. N. Lavagnino, B. X. Li, Y. Liang, E. Mao, A. Millet, J. V. Oakley, N. L. Reed, H. A. Sakai, C. P. Seath and D. W. C. MacMillan, *Chem. Rev.*, 2022, **122**, 1485–1542.
13 J. K. McCusker, *Science*, 2019, **363**, 484–488.
14 Y. Liu, P. Persson, V. Sundström and K. Wärnmark, *Acc. Chem. Res.*, 2016, **49**, 1477–1485.
15 N. Kaul, E. Asempa, J. A. Valdez-Moreira, J. M. Smith, E. Jakubikova and L. Hammarström, *J. Am. Chem. Soc.*, 2024, **146**, 24619–24629.
16 J. Wellauer, B. Pfund, I. Becker, F. Meyer, A. Prescimone and O. S. Wenger, *J. Am. Chem. Soc.*, 2025, **147**, 8760–8768.
17 K. S. Kjær, N. Kaul, O. Prakash, P. Chábera, N. W. Rosemann, A. Honarfar, O. Gordivska, L. A. Fredin, K.-E. Bergquist, L. Häggström, T. Ericsson, L. Lindh, A. Yartsev, S. Styring, P. Huang, J. Uhlig, J. Bendix, D. Strand, V. Sundström, P. Persson, R. Lomoth and K. Wärnmark, *Science*, 2019, **363**, 249–253.
18 S. Kronenberger, R. Naumann, C. Förster, N. R. East, J. Klett and K. Heinze, *Nat. Commun.*, 2025, **16**, 7850.
19 S. M. Fatur, S. G. Shepard, R. F. Higgins, M. P. Shores and N. H. Damrauer, *J. Am. Chem. Soc.*, 2017, **139**, 4493–4505.
20 M. Darari, A. Francés-Monerris, B. Marekha, A. Doudouh, E. Wenger, A. Monari, S. Haacke and P. C. Gros, *Molecules*, 2020, **25**, 5991.
21 A. Britz, W. Gawelda, T. A. Assefa, L. L. Jamula, J. T. Yarranton, A. Galler, D. Khakhulin, M. Diez, M. Harder, G. Doumy, A. M. March, É. Bajnóczi, Z. Németh, M. Pápai, E. Rozsályi, D. Sárosiné Szemes,

H. Cho, S. Mukherjee, C. Liu, T. K. Kim, R. W. Schoenlein, S. H. Southworth, L. Young, E. Jakubikova, N. Huse, G. Vankó, C. Bressler and J. K. McCusker, *Inorg. Chem.*, 2019, **58**, 9341–9350.

22 P. Dierks, Y. Vukadinovic and M. Bauer, *Inorg. Chem. Front.*, 2022, **9**, 206–220.

23 Z. J. Knepp, G. M. Repa and L. A. Fredin, *Chem. Phys. Rev.*, 2025, **6**, 021304.

24 J. T. Yarranton and J. K. McCusker, *J. Am. Chem. Soc.*, 2022, **144**, 12488–12500.

25 M. O. J. Y. Hunault, Y. Harada, J. Miyawaki, J. Wang, A. Meijerink, F. M. F. de Groot and M. M. van Schooneveld, *J. Phys. Chem. A*, 2018, **122**, 4399–4413.

26 R. M. Jay, K. Kunnus, P. Wernet and K. J. Gaffney, *Annu. Rev. Phys. Chem.*, 2022, **73**, 187–208.

27 C. B. Larsen, J. D. Braun, I. B. Lozada, K. Kunnus, E. Biasin, C. Kolodziej, C. Burda, A. A. Cordones, K. J. Gaffney and D. E. Herbert, *J. Am. Chem. Soc.*, 2021, **143**, 20645–20656.

28 A. W. Hahn, B. E. Van Kuiken, V. G. Chilkuri, N. Levin, E. Bill, T. Weyhermüller, A. Nicolaou, J. Miyawaki, Y. Harada and S. DeBeer, *Inorg. Chem.*, 2018, **57**, 9515–9530.

29 J. Steube, A. Kruse, O. S. Bokareva, T. Reuter, S. Demeshko, R. Schoch, M. A. Argüello Cordero, A. Krishna, S. Hohloch, F. Meyer, K. Heinze, O. Kühn, S. Lochbrunner and M. Bauer, *Nat. Chem.*, 2023, **15**, 468–474.

30 K. Kunnus, M. Vacher, T. C. B. Harlang, K. S. Kjær, K. Haldrup, E. Biasin, T. B. van Driel, M. Pápai, P. Chabera, Y. Liu, H. Tatsuno, C. Timm, E. Källman, M. Delcey, R. W. Hartsock, M. E. Reinhard, S. Koroidov, M. G. Laursen, F. B. Hansen, P. Vester, M. Christensen, L. Sandberg, Z. Németh, D. S. Szemes, É. Bajnóczi, R. Alonso-Mori, J. M. Glownia, S. Nelson, M. Sikorski, D. Sokaras, H. T. Lemke, S. E. Canton, K. B. Møller, M. M. Nielsen, G. Vankó, K. Wärnmark, V. Sundström, P. Persson, M. Lundberg, J. Uhlig and K. J. Gaffney, *Nat. Commun.*, 2020, **11**, 634.

31 A. Hofmann, L. Dahlenburg and R. van Eldik, *Inorg. Chem.*, 2003, **42**, 6528–6538.

32 E. C. Wasinger, F. M. F. de Groot, B. Hedman, K. O. Hodgson and E. I. Solomon, *J. Am. Chem. Soc.*, 2003, **125**, 12894–12906.

33 S. J. George, J. Fu, Y. Guo, O. B. Drury, S. Friedrich, T. Rauchfuss, P. I. Volkers, J. C. Peters, V. Scott, S. D. Brown, C. M. Thomas and S. P. Cramer, *Inorg. Chim. Acta*, 2008, **361**, 1157–1165.

34 R. V. Pinjari, M. G. Delcey, M. Guo, M. Odelius and M. Lundberg, *J. Chem. Phys.*, 2014, **141**, 124116.

35 K. Kunnus, W. Zhang, M. G. Delcey, R. V. Pinjari, P. S. Miedema, S. Schreck, W. Quevedo, H. Schröder, A. Föhlisch, K. J. Gaffney, M. Lundberg, M. Odelius and P. Wernet, *J. Phys. Chem. B*, 2016, **120**, 7182–7194.

36 C. Van Stappen, B. E. Van Kuiken, M. Mörtel, K. O. Ruotsalainen, D. Maganas, M. M. Khusniyarov and S. DeBeer, *Inorg. Chem.*, 2024, **63**, 7386–7400.

37 A. W. Hahn, B. E. Van Kuiken, M. al Samarai, M. Atanasov, T. Weyhermüller, Y.-T. Cui, J. Miyawaki, Y. Harada, A. Nicolaou and S. DeBeer, *Inorg. Chem.*, 2017, **56**, 8203–8211.

38 F. M. F. de Groot, H. Elnaggar, F. Frati, R.-p. Wang, M. U. Delgado-Jaime, M. van Veenendaal, J. Fernandez-Rodriguez, M. W. Haverkort, R. J. Green, G. van der Laan, Y. Kvashnin, A. Hariki, H. Ikeno, H. Ramanantoanina, C. Daul, B. Delley, M. Odelius, M. Lundberg, O. Kuhn, S. I. Bokarev, E. Shirley, J. Vinson, K. Gilmore, M. Stener, G. Fronzoni, P. Decleva, P. Kruger, M. Retegan, Y. Joly, C. Vorwerk, C. Draxl, J. Rehr and A. Tanaka, *J. Electron Spectrosc. Relat. Phenom.*, 2021, **249**, 147061.

39 R. K. Hocking, E. C. Wasinger, F. M. F. de Groot, K. O. Hodgson, B. Hedman and E. I. Solomon, *J. Am. Chem. Soc.*, 2006, **128**, 10442–10451.

40 Y. Tanabe and S. Sugano, *J. Phys. Soc. Jpn.*, 1954, **9**, 753–766.

41 K. Kunnus, L. Li, C. J. Titus, S. J. Lee, M. E. Reinhard, S. Koroidov, K. S. Kjær, K. Hong, K. Ledbetter, W. B. Doriese, G. C. O'Neil, D. S. Swetz, J. N. Ullom, D. Li, K. Irwin, D. Nordlund, A. A. Cordones and K. J. Gaffney, *Chem. Sci.*, 2020, **11**, 4360–4373.

42 H.-H. Schmidtke, in *Optical Spectra and Chemical Bonding in Inorganic Compounds: Special Volume dedicated to Professor Jørgensen I*, ed. D. M. P. Mingos and T. Schönherr, Springer Berlin Heidelberg, Berlin, Heidelberg, 2004, pp. 19–35, DOI: 10.1007/b11303.

43 M. Pápai, G. Vankó, T. Rozgonyi and T. J. Penfold, *J. Phys. Chem. Lett.*, 2016, **7**, 2009–2014.

44 B. N. Figgis and M. A. Hitchman, *Ligand Field Theory and Its Applications*, Wiley-VCH, New York, 2000, pp. 134–218.

45 N. Sinha, P. Yaltseva and O. S. Wenger, *Angew. Chem., Int. Ed.*, 2023, **62**, e202303864.

46 F. Reichenauer, D. Zorn, R. Naumann, C. Förster and K. Heinze, *Inorg. Chem.*, 2024, **63**, 23487–23496.

47 H. B. Gray and N. A. Beach, *J. Am. Chem. Soc.*, 1963, **85**, 2922–2927.

48 M. Abrahamsson, H. Wolpher, O. Johansson, J. Larsson, M. Kritikos, L. Eriksson, P.-O. Norrby, J. Bergquist, L. Sun, B. Åkermark and L. Hammarström, *Inorg. Chem.*, 2005, **44**, 3215–3225.

49 S. Otto, M. Grabolle, C. Förster, C. Kreitner, U. Resch-Genger and K. Heinze, *Angew. Chem., Int. Ed.*, 2015, **54**, 11572–11576.

50 M. D. Kuz'min, A. Savoyant and R. Hayn, *J. Chem. Phys.*, 2013, **138**, 244308.

51 C. K. Jørgensen, *Orbitals in Atoms and Molecules*, Academic Press, London, New York, 1962.

52 T. G. Burrow, N. M. Alcock, M. S. Huzan, M. A. Dunstan, J. A. Seed, B. Detlefs, P. Glatzel, M. O. J. Y. Hunault, J. Bendix, K. S. Pedersen and M. L. Baker, *J. Am. Chem. Soc.*, 2024, **146**, 22570–22582.

53 R. Hoffmann, S. Alvarez, C. Mealli, A. Falceto, T. J. Cahill III, T. Zeng and G. Manca, *Chem. Rev.*, 2016, **116**, 8173–8192.

54 A. M. Fatta and R. L. Lintvedt, *Inorg. Chem.*, 1972, **11**, 88–92.

55 C. E. Johnson, M. Deegbey, A. Ilic, N. Kaul, O. Prakash, K. Wärnmark, E. Jakubikova and R. Lomoth, *Dalton Trans.*, 2025, **54**, 3586–3590.

56 P. Chábera, K. S. Kjaer, O. Prakash, A. Honarfar, Y. Liu, L. A. Fredin, T. C. B. Harlang, S. Lidin, J. Uhlig,

V. Sundström, R. Lomoth, P. Persson and K. Wärnmark, *J. Chem. Phys. Lett.*, 2018, **9**, 459–463.
57 W. Leis, M. A. Argüello Cordero, S. Lochbrunner, H. Schubert and A. Berkefeld, *J. Am. Chem. Soc.*, 2022, **144**, 1169–1173.
58 M. E. Reinhard, B. K. Sidhu, I. B. Lozada, N. Powers-Riggs, R. J. Ortiz, H. Lim, R. Nickel, J. v. Lierop, R. Alonso-Mori, M. Chollet, L. B. Gee, P. L. Kramer, T. Kroll, S. L. Raj, T. B. van Driel, A. A. Cordones, D. Sokaras, D. E. Herbert and K. J. Gaffney, *J. Am. Chem. Soc.*, 2024, **146**, 17908–17916.
59 J. T. Malme, R. A. Clendening, R. Ash, T. Curry, T. Ren and J. Vura-Weis, *J. Am. Chem. Soc.*, 2023, **145**, 6029–6034.
60 R. T. Magar, M. T. Fortunato, G. M. Curtin, M. Deegbey, M. Romero, S. G. Maez, E. Jakubikova, C. Turro and J. J. Rack, *Chem. Commun.*, 2025, **61**, 19489–19492.
61 I. M. Dixon, S. Khan, F. Alary, M. Boggio-Pasqua and J. L. Heully, *Dalton Trans.*, 2014, **43**, 15898–15905.
62 O. Prakash, L. Lindh, N. Kaul, N. W. Rosemann, I. B. Losada, C. Johnson, P. Chábera, A. Ilic, J. Schwarz, A. K. Gupta, J. Uhlig, T. Ericsson, L. Häggström, P. Huang, J. Bendix, D. Strand, A. Yartsev, R. Lomoth, P. Persson and K. Wärnmark, *Inorg. Chem.*, 2022, **61**, 17515–17526.
63 J. Wellauer, F. Ziereisen, N. Sinha, A. Prescimone, A. Velić, F. Meyer and O. S. Wenger, *J. Am. Chem. Soc.*, 2024, **147**, 8760–8768.
64 A. Mishra, K. Sharma, C. E. Johnson, E. A. Fosu, J. Schwarz, O. Prakash, A. K. Gupta, P. Huang, F. Lindgren, L. Häggström, J. Bendix, E. Jakubikova, R. Lomoth and K. Wärnmark, *Chem. – Eur. J.*, 2025, **31**, e01985.
65 L. A. Fredin, M. Pápai, E. Rozsályi, G. Vankó, K. Wärnmark, V. Sundström and P. Persson, *J. Phys. Chem. Lett.*, 2014, **5**, 2066–2071.
66 R. A. Marcus and N. Sutin, *Biochim. Biophys. Acta, Rev. Bioenerg.*, 1985, **811**, 265–322.